Heavy Rainfall in Paraguay during the 2015/16 Austral Summer: Causes and Subseasonal-to-Seasonal Predictive Skill

JAMES DOSS-GOLLIN

Columbia Water Center, and Department of Earth and Environmental Engineering, Columbia University, New York, New York

ÁNGEL G. MUÑOZ

Atmospheric and Oceanic Sciences, Princeton University, Princeton, New Jersey, and International Research Institute for Climate and Society, The Earth Institute, Columbia University, Palisades, New York

SIMON J. MASON

International Research Institute for Climate and Society, The Earth Institute, Columbia University, Palisades, New York

MAX PASTÉN

Dirección de Meteorología e Hidrología, Asunción, and Facultad Politécnica, Universidad Nacional de Asunción, San Lorenzo, Paraguay

(Manuscript received 27 November 2017, in final form 7 May 2018)

ABSTRACT

During the austral summer 2015/16, severe flooding displaced over 170 000 people on the Paraguay River system in Paraguay, Argentina, and southern Brazil. These floods were driven by repeated heavy rainfall events in the lower Paraguay River basin. Alternating sequences of enhanced moisture inflow from the South American low-level jet and local convergence associated with baroclinic systems were conducive to mesoscale convective activity and enhanced precipitation. These circulation patterns were favored by cross-time-scale interactions of a very strong El Niño event, an unusually persistent Madden–Julian oscillation in phases 4 and 5, and the presence of a dipole SST anomaly in the central southern Atlantic Ocean. The simultaneous use of seasonal and subseasonal heavy rainfall predictions could have provided decision-makers with useful information about the start of these flooding events from two to four weeks in advance. Probabilistic seasonal forecasts available at the beginning of November successfully indicated heightened probability of heavy rainfall (90th percentile) over southern Paraguay and Brazil for December–February. Raw subseasonal forecasts of heavy rainfall exhibited limited skill at lead times beyond the first two predicted weeks, but a model output statistics approach involving principal component regression substantially improved the spatial distribution of skill for week 3 relative to other methods tested, including extended logistic regressions. A continuous monitoring of climate drivers impacting rainfall in the region, and the use of statistically corrected heavy precipitation seasonal and subseasonal forecasts, may help improve flood preparedness in this and other regions.

1. Introduction

During the austral summer of 2015/16, repeated heavy rainfall events led to severe flooding in the lower Paraguay River basin (LPRB) (Figs. 1 and 2), displacing approximately 170 000 people (Brakenridge 2016) and causing tremendous damage to property and infrastructure (Ministerio de Obras Públicas y Comunicación 2016). Because population in South America tends to concentrate along coasts and rivers (Fig. S1 in the supplemental material), flooding in the LPRB directly affects not only much of the population of Paraguay, but also of populations in Argentina and Uruguay along the Paraná and La Plata Rivers, into which the Paraguay River drains. Heavy rainfall and flooding in the LPRB also has important implications for hydropower generation, agriculture, and

Supplemental information related to this paper is available at the Journals Online website: https://doi.org/10.1175/JCLI-D-17-0805.s1.

Corresponding author: James Doss-Gollin, james.doss-gollin@columbia.edu

DOI: 10.1175/JCLI-D-17-0805.1

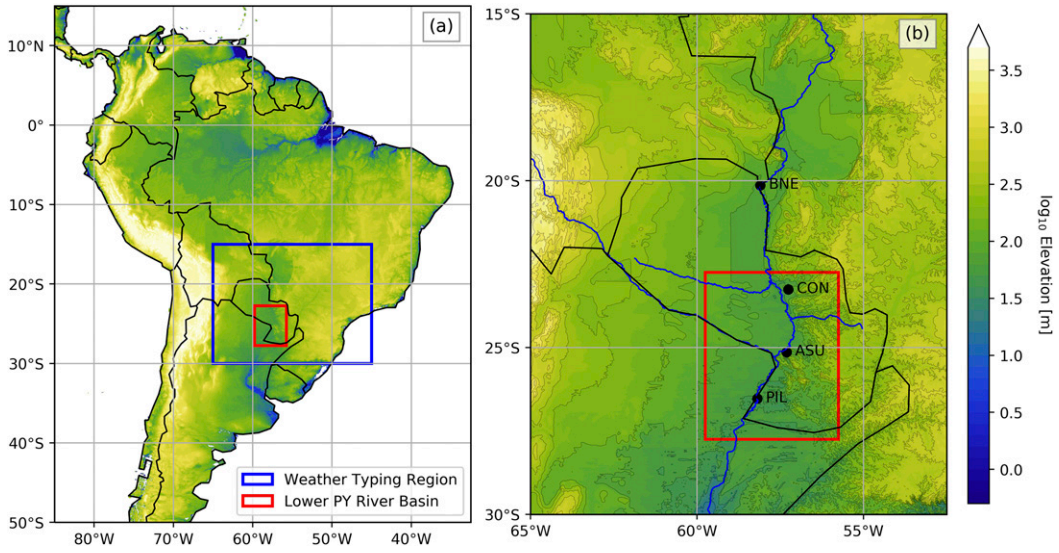

FIG. 1. Topographical map of the study area. Colors indicate $\log_{10}$ of elevation (m) from the Global Land 1-km Base Elevation Project (available online at http://iridl.ldeo.columbia.edu/SOURCES/.NOAA/.NGDC/.GLOBE/.topo/). (a) All of South America, with the domains of the LPRB and the domain used for weather typing indicated in red and blue boxes, respectively. (b) As in (a), the LPRB is marked with a red box. (Streamflow time series shown in Fig. 3 were taken from the four stations indicated.) The Paraguay River and its tributaries, from the Natural Earth Database (www.naturalearthdata.com), are also shown in (b). Stations shown are Bahía Negra (BNE), Concepción (CON), Asunción (ASU), and Pilar (PIL).

regional water resource management. The aim of this paper is to diagnose the drivers of the November–February (NDJF) 2015/16 rainfall and flooding events and to assess the skill of the relevant subseasonal-to-seasonal predictions.

The climatology of the LPRB varies strongly by season, with extratropical characteristics in the winter and monsoonal characteristics in the summer. The most notable circulation features during the warm season (NDJF), which is the focus of this study, are the upper-tropospheric Bolivian high, the lower-level subtropical highs, the Chaco low over northern Argentina, the South Atlantic convergence zone (SACZ), and the South American low-level jet (SALLJ) (Grimm and Zilli 2009; Marengo et al. 2012). Rainfall peaks around 5 mm day^{-1} during the warm

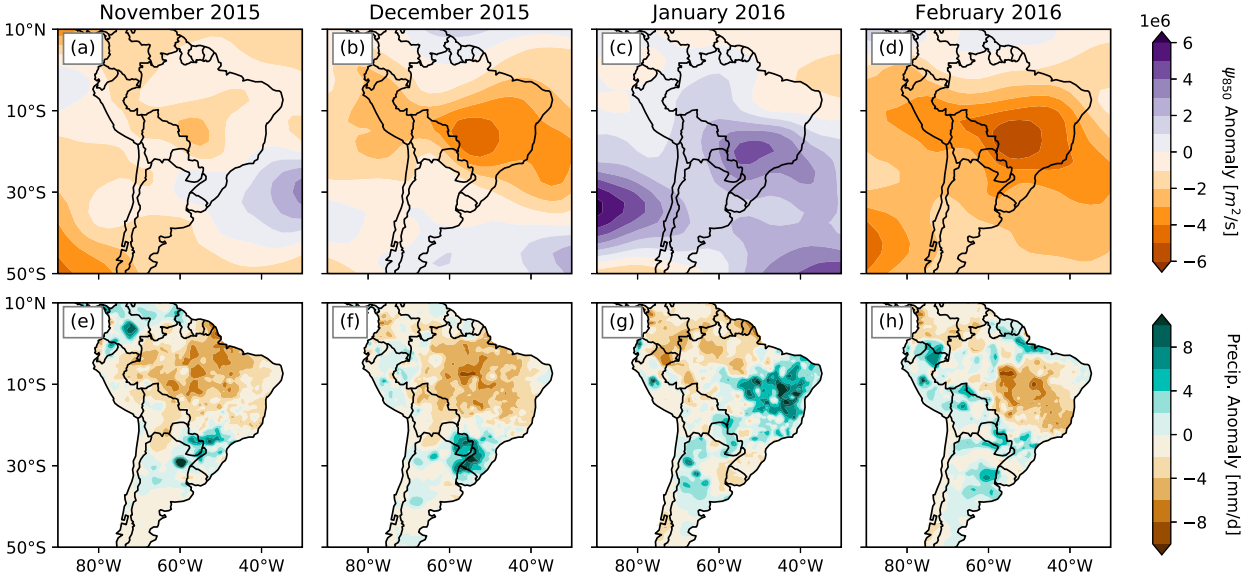

FIG. 2. Monthly composite anomalies observed during NDJF 2015/16, for (a)–(d) ψ_{850} (10^6 m^2 s^{-1}) and (e)–(h) rainfall (mm day^{-1}).

months (October–May) and reaches a minimum near 2 mm day^{-1} in July and August. However, the flat topography limits the river's ability to carry the summer runoff, causing seasonal inundation of the Pantanal and distributing the river discharge in time (Bravo et al. 2011; Barros et al. 2004). Thus, upstream of the Pantanal the streamflow maxima typically occur in phase with precipitation, while downstream of the Pantanal—an area that we define in Fig. 1 as the lower Paraguay River basin—the annual peak typically occurs between April and July.

During the warm season, a large fraction of rainfall, and nearly all heavy rainfall, in the LPRB is associated with mesoscale convection (Velasco and Fritsch 1987). Previous studies of organized convection and precipitation across subtropical continental South America have found close correspondence with the exit region of the low-level jets (Velasco and Fritsch 1987; Marengo et al. 2004; Saulo et al. 2007; Salio et al. 2007), which is influenced in both summer and winter by midlatitude baroclinic wave trains that interact with the Andes topography to generate orographically bound cyclones and northerly low-level flow (Campetella and Vera 2002; Seluchi et al. 2006; Boers et al. 2013, 2014). The strength and direction of this moisture transport varies substantially between events, and SALLJ exit regions range from central Argentina (Chaco jet events; Salio 2002) to Paraguay and southeastern Brazil (no-Chaco jet events; Vera et al. 2006).

At subseasonal time scales, heavy rainfall and convection in the LPRB is modulated by a variety of drivers, notably including the SACZ and the Madden–Julian oscillation (MJO). During SACZ conditions, strong low-level convergence is observed over the Amazon basin with low-level divergence over southwestern Brazil, northern Argentina, and Paraguay (Herdies 2002; Carvalho et al. 2011a); the opposite is true for so-called no-SACZ conditions. SACZ occurrence is related to westerly wind regimes over southeastern South America, as well as ''active'' and ''break'' periods of the South American monsoon system (Marengo et al. 2004). The MJO has been associated with the South American ''seesaw'' pattern (Nogués-Paegle and Mo 1997; Nogués-Paegle et al. 2000; Liebmann et al. 2004) and has been identified as a source of rainfall predictability for the region (e.g., Muñoz et al. 2015).

At seasonal time scales, El Niño–Southern Oscillation (ENSO) is the dominant driver of convection variability in the LPRB. During El Niño years, a low-level anticyclonic anomaly over central Brazil enhances occurrence of the low-level jet, favoring the development of mesoscale convective systems (Velasco and Fritsch 1987). The intensity and precise extent of this anomaly is relevant for the impact of ENSO events. The region also exhibits substantial rainfall variability between El Niño years, including a reversal of rainfall anomalies between November of that year and January of the following one, influenced by land surface interactions (Grimm 2003; Grimm and Zilli 2009). Even beyond El Niño years, regional land surface feedbacks can cause regions that exhibit wet anomalies in the spring to experience more summer precipitation on average (Grimm et al. 2007). Similarly, midlatitude dynamics influence low-level wind anomalies on many time scales, even though analysis of this relationship is complicated because of coupled tropical–extratropical interactions (Jones and Carvalho 2002; Carvalho et al. 2004). To address these potential interactions, a cross-time-scale approach based on synoptic circulation types is employed here to diagnose the causes of the rainfall events. This method has been used in previous work for southeastern South America (Muñoz et al. 2015, 2016a) and other regions (Moron et al. 2015).

The paper proceeds as follows. We first describe our data sources in section 2 and our methods in section 3. In section 4 we start our diagnosis, highlighting the observed flooding and contextualizing it within a long river stage time series; we then use composites and a weather-typing analysis to diagnose the circulation patterns associated with the heavy rainfall during NDJF 2015/16. We turn in section 5 to the question of whether the observed rainfall was successfully predicted by available models. To carry out this analysis, we study both forecasts targeting the entire series for a limited area, and also forecasts targeting a large spatial area for only the first week of December, when the most important flooding events began. We also explore the impact on forecasts of several bias-correction schemes. In section 6 we discuss limitations and potential implications of our findings and potential future work, and we present our concluding remarks in section 7.

2. Data

a. Observations

The period analyzed for diagnostic purposes is from 1 November 1979 through 28 February 2016. Figure 1 shows the study area and defines several spatial domains that are discussed throughout the paper.

Rainfall data are taken from the CPC unified gauge-based analysis of global daily precipitation dataset (Chen et al. 2008). Spatial resolution is 0.5° in latitude/longitude, and temporal resolution is daily. We define ''heavy'' rainfall events to be exceedances of the 90th percentile; while the value is different for each grid cell,

the 90th percentile of area-averaged rainfall over the LPRB is approximately 15 mm day^{-1}.

Atmospheric circulations are diagnosed using daily data from the NCEP–DOE AMIP-II reanalysis dataset (Kanamitsu et al. 2002). Spatial resolution is 2.5°. Because the end-of-day time for the rainfall data is 1200 UTC over most of South America (Chen et al. 2008), we use 6-h reanalysis data and shift by 12 h before resampling to the daily time step. This ensures that the time steps in the reanalysis and rainfall datasets are the same, but means that a day is defined as beginning at 1200 UTC. Since most summer rainfall in this region occurs overnight (Vera et al. 2006; Salio et al. 2007), this end-of-day time (which translates to approximately 0800 LT, depending on the exact time zone) tends to separate distinct events. The primary atmospheric variable used was the 850-hPa streamfunction, calculated directly from the wind field as described in section 3. The streamfunction is preferable to, for example, the geopotential height Φ because Φ has weak gradients near the equator, making it difficult to visualize circulations that span from the tropics to the extratropics. Data at 850 hPa was used because it is representative of SALLJ activity and moisture transport in this region (Marengo et al. 2004; Salio et al. 2007).

Oceanic sea surface temperature (SST) patterns are explored at the monthly time step using the 1° NOAA OISST version 2 dataset (Reynolds et al. 2002).

Streamflow data were collected by the Paraguayan Navy and National Administration of Navigation and Ports of Paraguay and were processed and distributed by the Paraguayan Directorate of Meteorology and Hydrology. Locations of streamflow gauges are shown in Fig. 1. Because no stage-discharge curves are available, we present only the river stage values; while this is relevant from the perspective of flood damage, flow rates cannot be estimated without these curves (which are difficult to reconstruct as river geometry changes over time).

This study also makes use of some climate indices. Data on ENSO, specifically the Niño-3.4 index, came from a statistical–dynamical interpolation (Kaplan et al. 1998), which is constrained by relatively high-quality observations during the study period. Data on the MJO came from the Australian Bureau of Meteorology (Wheeler and Hendon 2004).

b. *Model forecasts*

This study analyzes probabilistic seasonal and subseasonal forecasts of heavy rainfall events, which we define as exceedance of the 90th percentile of NDJF daily precipitation across all ensemble members and initializations.

The seasonal predictions used are known as "flexible format" forecasts, provided by the International Research Institute for Climate and Society (IRI). These forecasts use a multimodel ensemble approach, with bias-corrected retrospective probabilistic forecasts produced using a total of 144 members forced by evolving SSTs and 68 members forced by persisted SSTs; for details, see Barnston et al. (2010). Flexible format means that the user of these forecasts can arbitrarily choose particular thresholds (percentiles) to compute the probability of exceedance (or nonexceedance) from the complete probability density function of the climatological distribution, rather than using the more common tercile categories. The DJF 2015/16 forecasts analyzed were produced in November 2015. Because of the short sample of flexible format forecasts available (only for 2012–16 at the time of writing this paper), no verification was performed for these seasonal predictions. These forecasts are provided at a horizontal resolution of 2.5°. The DJF 2015/16 forecasts analyzed were produced in November 2015.

The subseasonal forecasts used were issued by the European Centre for Medium-Range Weather Forecasts (ECMWF) using the IFS cycle 41r1 coupled model. These forecasts are available via the Subseasonal to Seasonal (S2S) Prediction Project Database (Vitart et al. 2017) at 1.5° resolution. Forecasts consider the period starting in December 2015 until March 2016, and hindcasts to assess the real-time predictive skill consider the period 1–7 December in 1995–2014. There are a total of 51 ensemble members for each forecast, and 11 ensemble members for each of the 20 hindcasts.

Hindcasts were used to define the significant event threshold and for probabilistic forecast verification; forecasts were used to analyze modeled rainfall during the entire NDJF 2015/16 season and in particular the week of 1–7 December 2015. For probabilistic analysis of the rainfall during the week of 1–7 December 2015, rainfall forecasts and hindcasts considered were initialized on 12 and 16 November 2015.

Anomalies were calculated relative to the seasonal mean from November 1979 to February 2016, and the anomalies thus contain information on intraseasonal variability.

3. Methods

Several types of analyses are used to diagnose the causes of the heavy rainfall events and to bias-correct and verify the forecasts. Computation was performed in the Python environment using stable open-source packages (Hunter 2007; McKinney 2010; van der Walt et al. 2011; Hoyer and Hamman 2017). [All codes to

reproduce or modify this analysis are available online at https://github.com/jdossgollin/PYFloods (maintained) and https://doi.org/10.5281/zenodo.1294280 (permanent)].

Given the behavior of the Paraguay River discussed above, we define the lower Paraguay River basin as the region bounded from 59.75° to 55.75°W and from 26.75° to 22.75°S, as shown in Fig. 1. In this region, given topography and previous studies (Barros et al. 2004; Bravo et al. 2011), one might hypothesize rainfall inputs to most closely correspond to river levels at the stream gauges in Fig. 1.

a. Weather typing

A cluster algorithm is used on daily data to diagnose mechanisms associated with the rainfall events of interest in this research. The clustering was performed on the daily NDJF 850-hPa streamfunction field ψ_{850} calculated by integrating the meridional and zonal wind fields using spherical harmonics, as implemented in the windspharm package (Dawson 2016), over the domain spanning from 15°to 30°S and from 65°to 45°W (Fig. 1).

To facilitate clustering (which tends to perform poorly in high-dimensional spaces), the NDJF anomaly field of ψ_{850} was projected onto its four leading empirical orthogonal functions (EOFs), accounting for >95% of the total observed variance. No meridional weighting was applied as the selected domain is relatively small and does not extend into high latitudes. Once the EOFs were calculated, the principal component time series were computed for each day and scaled to unit variance. This rescaling is not a necessary step; its effect is to treat all retained principal components as equally important, which provides relatively greater weight to EOF2, EOF3, and EOF4 than carrying out the clustering without rescaling. Although our approach of first selecting the number of EOFs to use and then choosing to scale them equally involves more subjective decisions than an approach without rescaling, in this case the resulting physical patterns described by the EOFs more closely represent patterns identified in the literature; this is further discussed in section 4.

Next, the K-means algorithm was used to assign a single cluster value to each day on record using the four-dimensional principal component time series. The K-means technique is a partitioning method that classifies all days in the study into a predefined number of clusters. The algorithm proceeds as follows:

1) Randomly choose K cluster centers $\mu_1^{(0)}, \ldots, \mu_K^{(0)}$ (where 0 refers to the 0th iteration).
2) Iterate until convergence, indexing each iteration with j:
   (i) Assign each observation x_i (day) to the nearest cluster center; we define this using the Euclidean distance but other measures, such as the Mahalanobis distance, could also be used:

$$m_i^{(j+1)} := \arg\min_{k \in 1,\ldots,K} \|x_i - \mu_k^{(j)}\|. \quad (1)$$

   (ii) Recompute the cluster centers as the mean of all points assigned to that cluster

$$\mu_k^{(j+1)} := \frac{1}{|\{i | m_i^{(j+1)} = k\}|} \sum_{i | m_i^{(j+1)} = k} x_i, \quad (2)$$

   where $|\cdot|$ denotes vector length.
   (iii) Stop iteration if the change in centroids $\mu^{(j+1)} - \mu^{(j)}$ is less than a small but nonzero tolerance parameter τ.

The cluster centroids μ_k produced by the K-means algorithm can then be interpreted as a Voronoi decomposition of the phase space into K regions, and specifically as the Voronoi diagram, which minimizes within-cluster variance.

The K-means algorithm is guaranteed to converge to a local minimum of intercluster variance; to select the best partition, 500 simulations were created using the implementation in Python's scikit-learn package (Pedregosa et al. 2011). Next, the classifiability index of Michelangeli et al. (1995) was computed between each partition and the 499 others. The partition whose classifiability index, averaged for all 499 pairwise comparisons, was the highest was selected. Calculation of the classifiability index for several values of K (Fig. S2 in the supplemental material) suggests that states with $K = 5, 6, \ldots, 8$ are all reasonable. We chose the solution $K = 6$ because the clusters identified are qualitatively similar to those determined over southeastern South America (Muñoz et al. 2015, 2016a) and have an intuitive physical meaning, which we discuss further in the following sections. We refer to the resulting clusters as weather types (WTs). From a physical point of view, the K-means algorithm helps identify typical atmospheric circulation patterns in the EOF-filtered field via clustering of days with similar streamfunction configurations. These clusters can also be understood as proxies of the available states of the system, or the most frequently visited trajectories in the phase space of the physical system (Muñoz et al. 2015, 2016b, 2017).

b. Forecasts and model output statistics

A wide variety of methods, generically known as model output statistics (MOS) (Glahn and Lowry 1972), have been proposed to correct for different types of bias in model output. In this work, we analyze how well the rainfall events could have been predicted, using both the

TABLE 1. MOS methods used to correct the ECMWF subseasonal forecasts. Spatial domain for predictand is always the same (39°–17°S, 66°–49°W). Two initializations are used: 12 and 16 Nov 2015.

Model	Region (predictor)	Final predictor(s) selected
Raw	39°–17°S, 66°–49°W	Ensemble mean, computed using members from the two initializations. No correction performed.
XLR	39°–17°S, 66°–49°W	Ensemble mean, computed using members from the two initializations.
HLXR	39°–17°S, 66°–49°W	Ensemble mean and spread, computed using members from the two initializations.
PCR	60°S–0°, 80°–30°W	Linear combination of model's EOFs computed using both initializations as independent predictors (10 EOFs).
CCA	60°S–0°, 80°–30°W	Canonical modes computed using both initializations as independent predictors (10 predictor and 4 predictand EOFs, 4 canonical modes).

raw subseasonal forecasts and MOS-adjusted subseasonal forecasts. We use four types of MOS techniques: homoscedastic extended logistic regression (XLR), heteroscedastic extended logistic regression (HXLR), principal components regression (PCR), and canonical correlation analysis (CCA).

Logistic regression models the probability of binary events, conditional on one or more predictors, and has been widely used in MOS. Nonetheless, when using logistic regression to address multiple thresholds via independent fits, the predicted probabilities are, in general, not mutually consistent (Messner et al. 2014). XLR was designed to address this shortcoming via the consideration of a transformation of the thresholds of interest as an additional predictor variable (Wilks 2009). HXLR, a generalization of the XLR, was proposed to appropriately use the ensemble spread as predictor for the dispersion of the predictive distribution (Messner et al. 2014).

CCA is a common statistical method frequently used to forecast rainfall using a purely empirical approach (Mason and Baddour 2008; Barnston et al. 2012; Jolliffe and Stephenson 2012; Barnston and Ropelewski 1992; Wilks 2006). CCA identifies modes of covariability, called canonical variates or canonical modes, by maximizing the correlation between linear combinations of the predictor and predictand's EOF. The method forecasts spatial patterns of variability spanning across the region of interest rather than making forecasts for individual locations. In PCR, a special case of CCA, each grid cell in the predictand field is estimated by regression using a linear combination of the predictor's EOFs (Mason and Baddour 2008; Wilks 2006) rather than by identifying canonical modes. Unlike XLR and HXLR models, which perform bias correction independently for each grid cell, CCA and PCR models can address biases in both the magnitude and the spatial distribution of the modeled precipitation patterns.

For the purposes of MOS corrections, the predictand (variable to be forecast) is the observed rainfall for the target period of interest, and the predictor (variable to be corrected) is the uncorrected S2S model forecast rainfall for the same period. Exceedance of the 90th percentile during the 1995–2014 period is used to define the heavy event cases. We use the same spatial domain (39°–17°S, 66°–49°W) for both the predictor and the predictand, except for the PCR and CCA cases, in which a larger domain (0°–60°S, 80°–30°W) was used to better capture the spatial patterns in the uncorrected S2S model forecast field. A variety of domains and ways to combine initialization times were explored; the best results were selected in terms of the corresponding Kendall's τ rank correlation coefficient between observations and hindcasts. A summary of the final candidate predictors found to be most skillful for each MOS model is presented in Table 1.

To evaluate model skill, we use a cross-validation approach with a 5-yr window. In this framework, five continuous years are left out of the record, the regression coefficients are computed with the remaining time series, and the resulting model is validated comparing the prediction for the third year left out (middle of the window) against observations. The 5-yr-long window is redefined a year at a time, moving from the beginning of the record to its end.

To visualize the probability of heavy rainfall at each grid cell, we present all predictions in terms of odds relative to the climatological odds:

$$\text{odds}_r \equiv \frac{p}{(1-p)} \frac{(1-p_c)}{p_c}, \tag{3}$$

where p and p_c represent the forecast probability for the exceedance of the 90th percentile and the related climatological probability, respectively.

As indicated earlier, the IRI's seasonal forecasts are already provided with spatial MOS corrections of systematic errors of the individual models in the ensemble via CCA (Barnston et al. 2010), and thus we did not perform any further MOS on the seasonal rainfall fields.

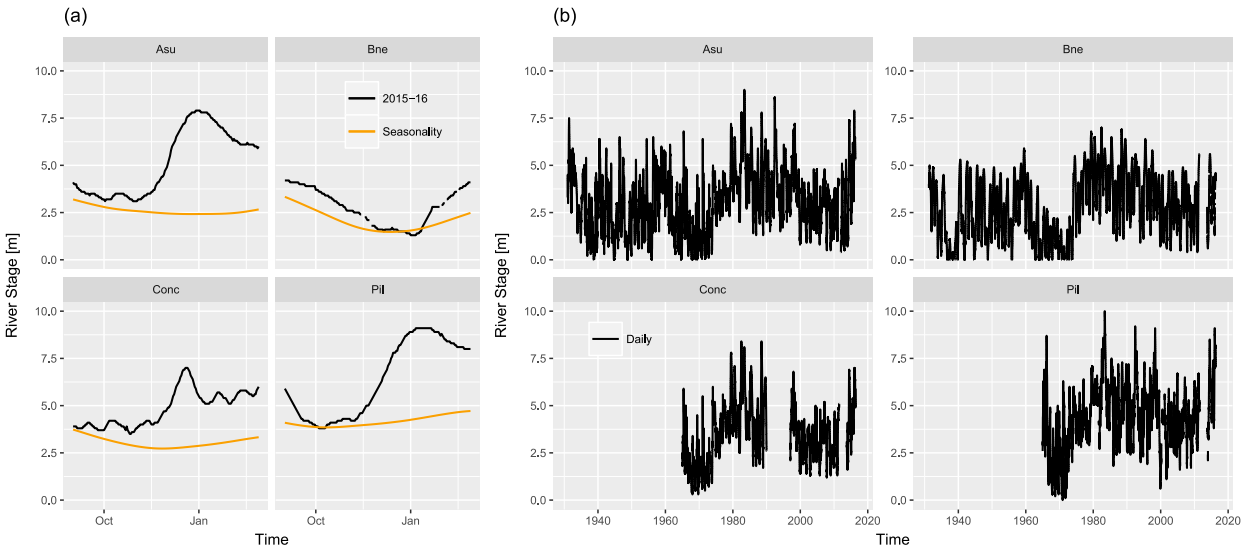

FIG. 3. River stage (height; m) for the Paraguay River at four gauges along the Paraguay River. The station names are those shown in Fig. 1. (a) Seasonality (orange) and time series of 2015/16 observations (black) at each stream gauge. Seasonality was fit using local polynomial regression as implemented in the locfit package in the R statistical programming environment (Loader 1999). (b) Time series of daily stage measurements from 1929 to 2016 at each station.

c. *Probabilistic forecast verification*

In addition to visually comparing predictions and observations to verify how well the heavy rainfall events could have been predicted, we use the ignorance score:

$$\mathrm{IGN} \equiv -\log_2 p(Y), \tag{4}$$

where Y is the observed outcome and $p(Y)$ is the density function of the forecast distribution (Good 1952; Roulston and Smith 2002; Bröcker and Smith 2007). The ignorance score was introduced as an information-theory-based verification measure, decomposable into easily interpretable components: reliability, resolution, and uncertainty (Weijs et al. 2010). Because of its close relationship to Shannon's information entropy, it is used to measure forecast utility, or the amount of information gain expected from a forecast (Roulston and Smith 2002).

We also compute the generalized relative operating characteristics score, also known as the two-alternative forced choice (2AFC) score (Mason and Weigel 2009), to evaluate skill of probabilistic rainfall forecasts. This score measures the proportion of all available pairs of observations of differing category whose probability forecasts are discriminated in the correct direction (Mason and Weigel 2009). It has an intuitive interpretation as an indication of how often the forecasts are correct.

These two metrics, measuring reliability, resolution, uncertainty, and discrimination, are deemed here to be sufficient to characterize the forecast skill for our events of interest. To conduct the verification in a consistent manner, we use the climate predictability tool, developed and maintained by the IRI (Mason and Tippett 2017).

4. Diagnostics

a. *Observed flooding*

Figure 3 shows the streamflow time series at several gauges on the Paraguay River during NDJF 2015/16 in the context of their seasonality and decadal variability. During November and December 2015, the river rose rapidly at Concepción, Asunción, and Pilar, although not at Bahía Negra. As discussed in Barros et al. (2004) and Bravo et al. (2011), the location of the Bahía Negra gauge (see Fig. 1) in the Pantanal region means that it responds very slowly to rainfall input. The three downstream gauges, because they are located in the LPRB, respond to the rainfall forcing with a slow but steady rise. Despite several very heavy storms, the streamflow record at Asunción and Pilar (which are downstream of Concepción) indicates relatively little response to individual storms. Because the region is so flat (see topographic data in Fig. 1), river levels at a particular point may be affected not only by rain in the catchment corresponding to that point, but also by elevated river levels downstream that reduce the pressure gradient available to drive flow.

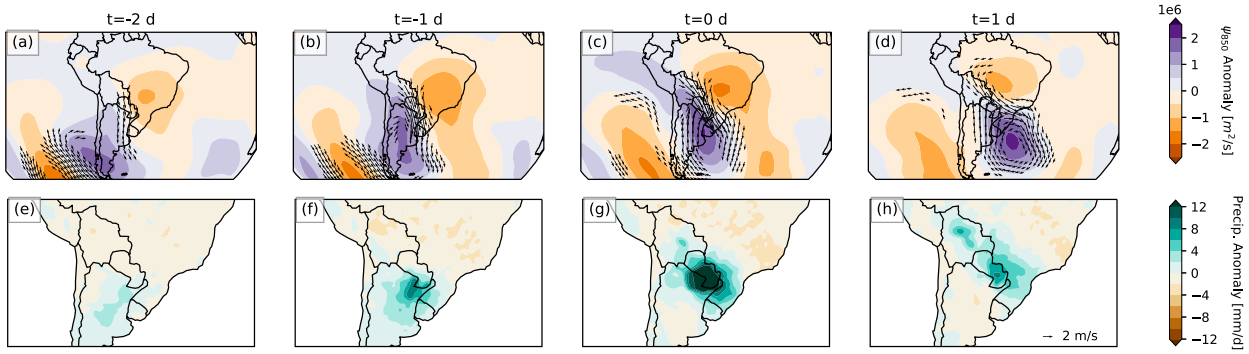

FIG. 4. Composite anomalies associated with heavy rainfall (90th percentile exceedance of area-averaged rainfall in the LPRB). Lagged composites are shown, for t = (a),(e) −2, (b),(f) −1, (c),(g) 0, and (d),(h) 1 day relative to the date of heavy rainfall. (top) Composite ψ_{850} (shading) and wind anomalies at 850 hPa (vectors), with the strongest 5% of wind anomaly vectors between 60°S and 10°N (all longitudes) are also shown, and (bottom) composite rainfall anomalies (mm day^{-1}).

Examination of Fig. 3b suggests multidecadal oscillation in the streamflow record. This is in agreement with previous studies (Collischonn et al. 2001; Carvalho et al. 2011b) that find a changepoint in the 1970s, possibly associated with low-frequency Pacific variability. Because only river stage data (and not discharge) are available, it is not possible to discern whether the observed changes in river stage are driven by sediment loading and local measurement characteristics or by large-scale climate fluctuations. Further treatment of this question is beyond the scope of this paper.

b. *Heavy rainfall: Climatological drivers*

To understand how circulation anomalies observed during NDJF 2015/16 led to the observed floods, it is helpful to first explore the atmospheric circulations that are typically associated with heavy rainfall in the lower Paraguay River in the full observed record.

Figure 4 shows time-lagged anomalies up to and after heavy rainfall dates (when area-averaged daily rainfall in the LPRB exceeds its NDJF 90th percentile) and is consistent with previous analysis of heavy rainfall and intense convection in this region (Liebmann et al. 2004; Marengo et al. 2004; Salio et al. 2007; Marwan and Kurths 2015). At $t = -2$ days a midlatitude baroclinic system approaches the South American continent, intensifying and moving to the east from −1 to 1 day. This system interacts with the subtropical low and the Andes to produce an anticyclonic anomaly over Brazil. Along this system's cold front, a low-level northerly jet advects heat and moisture to the region. As the system progresses, the jet below 20°S transitions from predominantly meridional flow (Chaco jet; $t = -1$ day) to predominantly zonal flow (no-Chaco jet; $t = 0$ day). The pattern resembles composites identified using one standard deviation exceedances of rainfall at 30°S, 60°W (Liebmann et al. 2004), and analysis for the 95th or 99th percentiles of daily rainfall (not shown) yield similar results, implying that the synoptic mechanism for the heaviest events is not fundamentally distinct from the mechanism for moderate-intensity events. This mean field, like all composites, masks between-event variation, but exploration of individual events (not shown) indicates that the core features identified are generally present.

c. *Weather type analysis: Daily circulation patterns*

We next use the weather-typing algorithm outlined in section 3a to understand particular circulations and sequences of circulations associated with heavy rainfall in the LPRB.

The first step of the weather-typing algorithm is to identify leading EOFs of the 850-hPa streamfunction. The EOF loadings are shown in Fig. 5. Of these, EOF1 explains a substantial amount of variance (~72%) while EOF2, EOF3, and EOF4 collectively explain approximately 27% of total variance. The resulting WTs, shown in Fig. 6, reveal patterns associated with synoptic- and regional-scale circulation regimes. This is consistent with the hypothesis that the EOFs of ψ_{850} over the study area are associated with large-scale patterns.

WT 1 describes a SALLJ event in which the strongest wind penetrates southward of 25°S, leading to heavy rainfall over northeastern Argentina and Uruguay; this has been called a Chaco jet event (Salio 2002). WT 4 also shows SALLJ activity, but the wind turns to the east northward of 25°S, leading to heavy rainfall over eastern Paraguay and southwestern Brazil; this has been called a no-Chaco jet event (Vera et al. 2006). Table S1 in the supplemental material shows the centroids of each cluster, in the four-dimensional phase space of the leading EOFs of 850-hPa streamfunction.

WTs 5 and 3 look to be nearly inverses of WTs 1 and 4, respectively, and are associated with dry anomalies over the LPRB. The fact that they are not exact inverses

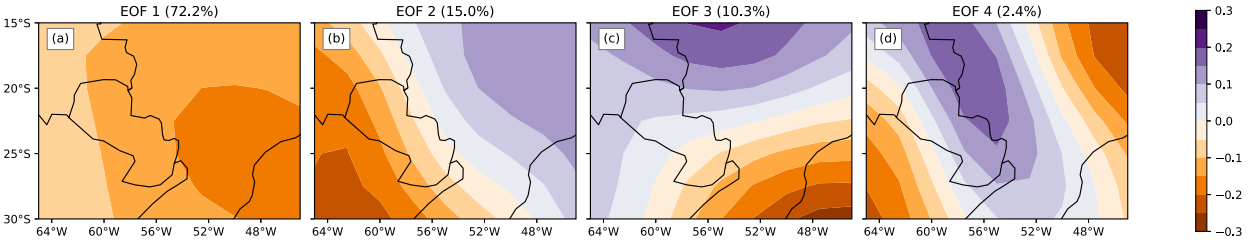

FIG. 5. Loadings of the four leading EOFs of daily NDJF ψ_{850} over the weather-typing region shown in Fig. 1. Parentheses in panel titles indicate the percentage of total variance explained by each EOF.

suggest important nonlinearities in the system. Weather types 1 and 5 resemble the two phases of the South American seesaw dipole, which is related to the SACZ (Nogués-Paegle and Mo 1997). Finally, WTs 2 and 6 are related to a high-pressure configuration bringing below-average rainfall over most of Brazil, and a dipole pattern conducive to above-average rainfall over central Brazil, respectively (Fig. 6).

d. NDJF 2015/16: Circulation sequences

We next use monthly-mean circulation anomalies (spatial patterns) and weather type sequences (temporal patterns) to understand the specific events of NDJF 2015/16.

While weather typing requires simplifying the dynamics of daily circulation patterns, its advantage is that it greatly facilitates the analysis of sequences of precipitation. Figure 7 shows a time series of area-averaged rainfall over the LPRB for NDJF 2015/16 and the corresponding weather types. This plot shows that heavy rainfall concentrated over a period spanning from mid-November 2015 through early January 2016, with shorter peaks in late January and mid-February.

As indicated in Fig. 7, the heaviest rainfall occurred during WTs 1 and 4. During NDJF 2015/16, WTs 1 and 4 (Chaco and no-Chaco jet extensions, respectively), occurred more frequently than their climatology (Table S2 in the supplemental material); WT 2 also occurred more frequently than its climatology, largely due to a long sequence in February 2016. In mid-January 2016, during a sequence of persistent low rainfall, multiple consecutive days of WT 3 were observed, leading to heavy rainfall over central Brazil (not shown) and dry conditions over the LPRB. Thus, while the intensity and persistence of heavy rainfall was atypical, the causal mechanism of the heavy rainfall observed during this season was consistent with climatology.

Inspection of Fig. 7 also suggests that at time scales of days to weeks, particular sequences of weather types tend to recur and are associated with repeated rainfall storms. From mid-November to late December 2015, nearly all days were weather types 1, 4, and 5, consistent with the anticyclonic anomaly observed over central Brazil during that time (Fig. 2). Nearly all of the heavy rainfall occurred during WTs 1 and 4. During mid-to-late January 2016, repeated WT 3 days led to persistent low rainfall, and in mid-February 2016 frequent occurrence of WT 2 led to frequent, although generally not intense, rainfall.

Transitioning from exploring the time evolution of the reduced-dimension system represented by the weather types, monthly-scale circulation anomalies (Fig. 2) show a weak anticyclonic circulation that set up over central Brazil during November 2015 and strengthened into the

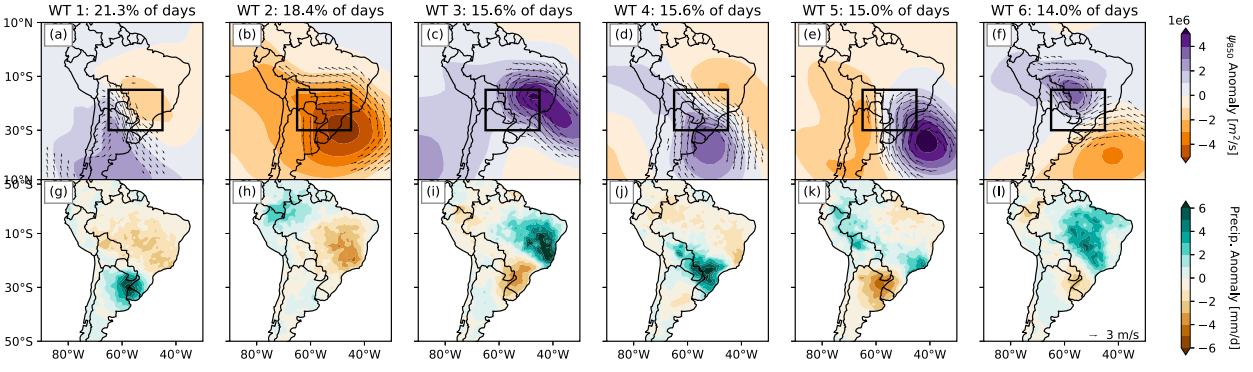

FIG. 6. Composite anomalies associated with each WT, for (a)–(f) ψ_{850} and wind anomalies at 850 hPa (vectors), with the strongest 20% of wind anomaly vectors over the plot area are also shown, and (g)–(l) rainfall anomalies (mm day^{-1}). The relative frequency of occurrence of each WT (in % of days) is presented above (a)–(f).

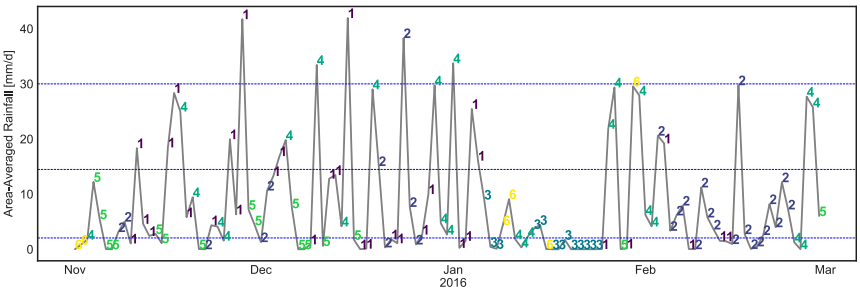

FIG. 7. Time series of area-averaged rainfall in the LPRB (see Fig. 1) for each day of NDJF 2015/16. Lines indicate the rainfall value (mm day^{-1}). The WT corresponding to each day is indicated by the adjacent text label. The horizontal dashed blue lines indicate, from bottom to top, the climatological 50th, 90th, and 99th percentiles, respectively, of NDJF area-averaged rain over the LPRB.

following month. In January 2016 it weakened before returning in February 2016. The observed rainfall and circulation anomalies are consistent with the aggregation of the observed weather types shown in Fig. 7 and discussed above.

5. Forecasts

In this section we analyze the extent to which forecasts were able to predict the persistent rainfall during summer of 2015/16. There are advantages in simultaneously considering useful climate information at multiple time scales, rather than just focusing on one of them (Hellmuth et al. 2011; Goddard et al. 2014). In this study we analyze probabilistic seasonal (DJF 2015/16) and subseasonal (1–7 December 2015) forecasts.

a. Seasonal forecast

Heavy rainfall over the region was forecast for the DJF 2015/16 season since at least November 2015 (see Fig. 8). Relative odds as high as 9:1 are visible over southern Paraguay and Brazil and northern Uruguay and Argentina, broadly in agreement with observations. The model predicted only very weakly increased odds of heavy rainfall in the Pantanal region (directly north of the LPRB) and northern Argentina at about 65°W and missed the heavy precipitation along most of the northeastern border of Paraguay. However, the regionally elevated forecast of heavy rainfall could have been used for disaster preparedness at least one month in advance, consistent with the El Niño signal.

b. Subseasonal forecasts

Subseasonal predictions are still too new to be used as operational tools, and their skill is normally not high enough to be useful for most decision-making (Vigaud et al. 2017). Nonetheless, the international S2S Prediction Project (Vitart et al. 2017) provides free access to almost-real-time subseasonal forecasts from multiple models, an opportunity to explore how well the heavy rainfall events of the first week of December 2015 could have been predicted.

Figure 9 (top) uses a Chiclet diagram (Carbin et al. 2016) to visualize, as a function of lead time, the time evolution of the uncorrected, ensemble-mean rainfall anomaly forecast, spatially averaged over the LPRB. At

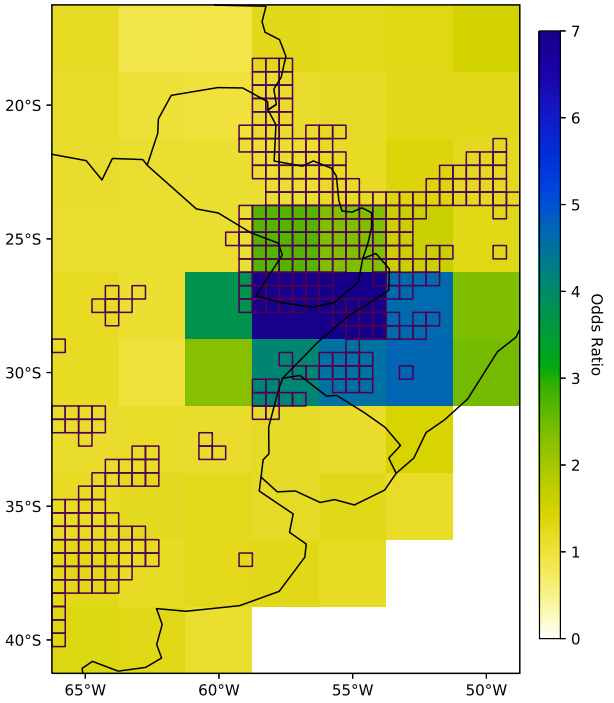

FIG. 8. Seasonal model forecast for probability of exceedance of 90th percentile of DJF rainfall, as issued in November 2015. Color indicates the forecast probability of exceeding the 90th percentile of climatological rainfall during DJF 2015/16—this is presented as odds$_r$ defined in Eq. (3). A value greater than 1 indicates that the model forecast greater-than-average odds of rainfall exceeding the 90th percentile. Grid cells that observed an exceedance of the 90th percentile of DJF rainfall are outlined in black.

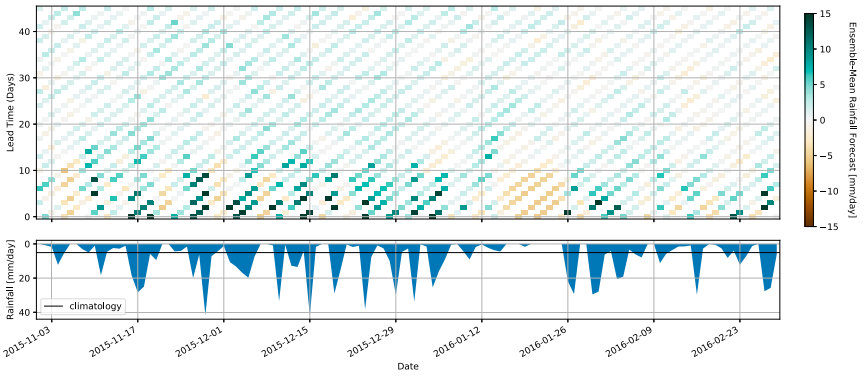

FIG. 9. (top) Chiclet diagram (see Carbin et al. 2016) of ensemble-mean precipitation anomaly forecasts over the LPRB (see Fig. 1) from uncorrected ECMWF S2S model forecast data, as a function of the forecast target date (horizontal axis) and lead time (vertical axis). (bottom) Time series of CPC daily mean precipitation over the same area is plotted with *y* axis inverted; horizontal black line denotes NDJF climatology.

times greater than about 2 weeks, the ensemble-mean forecast is for slightly positive rainfall anomalies at nearly all initialization dates and lead times. At weather time scales (less than 1 week), the ensemble mean successfully predicts the timing and amplitude of the area-averaged rainfall. At time scales of 1–3 weeks, the ensemble average successfully forecast the strongest breaks and pauses in the rainfall, such as the heavy rainfall during December 2015 and the dry period during mid-January 2016.

To examine these forecasts more closely, we turn to the 14–19-day forecast of the 1–7 December 2015 period. As seen in Fig. 10, the raw (uncorrected) subseasonal forecast of the ECMWF model for 1–7 December 2015 indicated very high relative odds for occurrence of heavy rainfall but with important biases in the actual location and spatial pattern; for Paraguay, it confidently suggests occurrence of heavy rainfall to the south-southeast of the country, which was mostly not observed. Overall, the 20-yr skill of probabilistic forecasts for the first week of December is highest over southern Brazil, parts of Argentina, and the western border of the domain under study (see Figs. 10f,k), but not over Paraguay. These skill scores indicate that the model is capturing a signal and suggest the use of MOS methods to explore the extent to which corrections in the magnitudes and spatial patterns may improve the forecast.

In general, the use of extended logistic regression models does not improve the forecast for the week. For example, with respect to the raw prediction, XLR tends to amplify the relative odds and to cluster and shift the forecast location of the heavy rainfall events (Figs. 10a,b); the forecast tends to be better for Uruguay, but suggests heavy rainfall in the Paraguayan Chaco, which was not present in the raw prediction. On the other hand, the use of the ensemble spread in the HXLR model does not help; this forecast tends to be overconfident on the events occurring in almost all the regions of interest (Fig. 10c).

Comparison of long-term skill between the uncorrected S2S model forecast output and both extended logistic regression models shows similar results. Reliability, resolution, and uncertainty, as measured by the ignorance score (Figs. 10f–h), suggests slight skill improvement in southern Brazil, deterioration in Argentina and Uruguay, and basically the same as the uncorrected S2S model forecast for Paraguay and southeastern Bolivia. Changes in forecast discrimination exhibited by the extended logistic models, as measured via the 2AFC score (Figs. 10k–m), are null. The extended logistic models operate on a gridbox-by-gridbox basis to recalibrate the probabilities, and so this recalibration happens monotonically. Since the 2AFC score is insensitive to monotonic transformations of forecasts, the forecast discrimination is unchanged.

Better forecasts are obtained when both magnitude and spatial corrections are performed, although with relative odds considerably less confident than the ones in the raw forecast. The PCR model correctly shows high relative odds in most of the places where heavy rainfall was observed (Fig. 10d), although it also indicates heightened risk in areas where heavy rainfall did not occur, like zones of western Paraguay and northeastern Argentina. The main problem with the CCA model is its lack of discrimination between occurrence or nonoccurrence of heavy rainfall in the region: the spatial distribution of odds is too homogeneous (Fig. 10e).

The 20-yr-based skill maps of probabilistic forecasts computed with these two EOF-based models are very similar to each other, both in terms of the reliability, resolution, and uncertainty measured by the ignorance score and the discrimination measured by the 2AFC score (Figs. 10i,j,n,o). In terms of long-term skill for the regions of interest over Paraguay, output from the PCR- and CCA-based MOS tend to

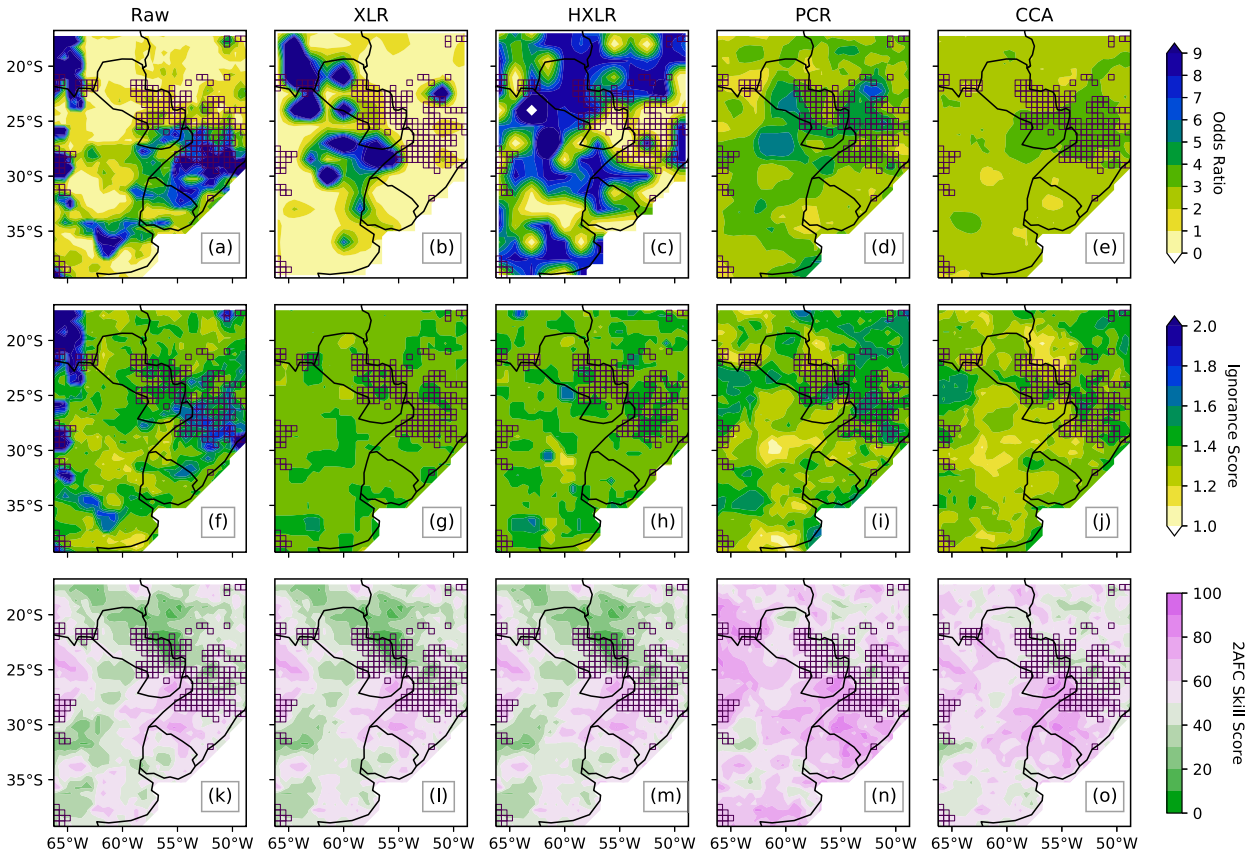

FIG. 10. Raw and MOS-adjusted S2S model forecasts and skill scores for the methods indicated in Table 1. (a)–(e) The heavy rainfall forecast for 1–7 Dec 2015 as odds, defined in Eq. (3) over the target domain. A value greater than 1 indicates that the model forecast greater-than-average odds of rainfall exceeding the 90th percentile. (f)–(j) The IGN defined in Eq. (4), with zero indicating a perfect forecast. (k)–(o) The 2AFC skill score for each grid cell; a value greater than 50 indicates that the model outperforms climatology. Different MOS models except for Raw in (a),(f),(k), which indicates the uncorrected S2S model output. In (top)–(bottom), the grid cells that observed a 90th percentile exceedance for 1–7 Dec 2015 are outlined in black.

outperform the raw forecasts and the extended logistic regression models, especially regarding discrimination (Figs. 10k–o). The enhanced skill is achieved through spatial corrections via the EOF-based regressions, which—in contrast with the extended logistic models—use information from multiple grid boxes, and thus the original forecasts are not necessarily calibrated monotonically.

Despite the particular errors in the 1–7 December 2015 forecasts, on the long term both PCR and CCA verify considerably better than the raw, XLR, and HXLR predictions. Yet despite the generally high skill score for these forecasts, there are still zones along the eastern part of Paraguay with lower discrimination skill than that of climatology.

6. Discussion

Co-occurrence of WTs 1 and 4, particularly in late November through late December 2015, favored advection of moisture and moist static energy into the LPRB, and low-level wind shear favored mesoscale convective activity, consistent with previous analyses in this region (Velasco and Fritsch 1987; Marengo et al. 2004; Saulo et al. 2007; Salio et al. 2007). Although many of the individual rainfall events of NDJF 2015/16 were intense, they were nonetheless driven by the climatological mechanism for heavy rainfall and intense convection shown in Fig. 4 rather than by some other extreme mechanism. Consequently, the most striking hydrometeorological feature of this season, likely a key driver of the observed flooding, was the persistence of the heavy rainfall and the manner in which it switched "on" and "off" over the study region (Fig. 7). In fact, this apparent on and off switching was manifest principally as a spatial shift in the rainfall occurrence (Fig. 2) consistent with the increased occurrence of WT 3 during mid-to-late January 2016 (Figs. 6 and 7); this pattern has been previously described as the South American seesaw pattern (Nogués-Paegle and Mo 1997).

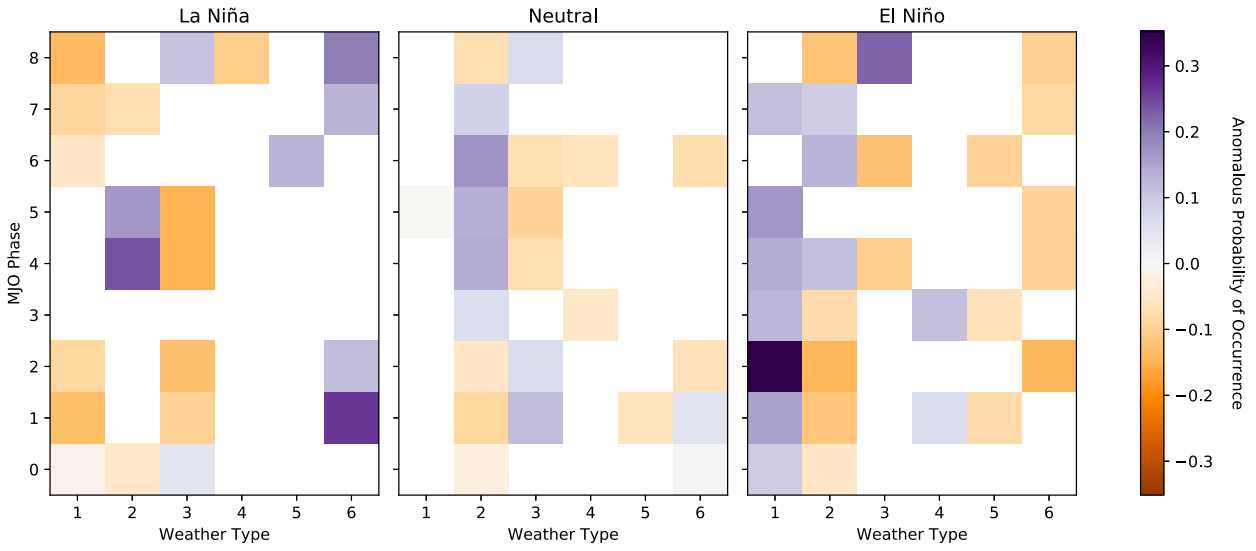

FIG. 11. Anomalous probability of occurrence of each WT concurrent with observance of each MJO phase. When MJO amplitude is less than 1, it is defined as neutral phase (0). Plots are shown separately for (left)–(right) La Niña (Niño-3.4 < -1), neutral ENSO, and El Niño (Niño-3.4 > 1) phases. Only values that are significant at $\alpha = 0.10$, calculated with a bootstrap of 5000 samples, are shown.

Although many news reports blamed the flooding on El Niño (British Broadcasting Corporation 2015), NDJF 2015/16 featured more intense rainfall than previous major El Niño events, and this intense rainfall persisted for a longer time. While the link between El Niño and flooding in the LPRB is consistent with previous studies of ENSO and summertime rainfall in this region (Velasco and Fritsch 1987; Grimm et al. 2000; Salio 2002; Grimm 2003; Carvalho et al. 2004; Grimm and Tedeschi 2009; Bravo et al. 2011), both the on and off switching and the differences from previous major El Niño events suggest that other physical mechanisms, and their cross-time-scale interactions, are relevant for understanding and predicting future events.

Figure 11 shows that WT 1 occurs more frequently during El Niño years for most MJO phases, particularly during phase 2. During El Niño years, WT 3—associated with dryness over the LPRB—occurs less frequently during MJO phases 4, 6, and 7 and more often during MJO phase 8; this is consistent with the lack of WT 3 during December 2015 and the frequent WT 3 occurrence in mid-January 2016 (Fig. 7). Detailed consideration of the role of MJO–ENSO interaction with circulation patterns over the study region is beyond the scope of this paper, but these two patterns provided background conditions favorable for the weather type sequences observed during NDJF 2015/16.

Through analysis of the relationship between relevant physical mechanisms and the occurrence probability of the identified weather types, it may be possible to better understand the drivers of this and future extreme event(s). As a starting point, we consider the joint role of ENSO, discussed above, and the MJO. During NDJF 2015/16, the Niño-3.4 index was strongly positive, representing a strong El Niño state (Figs. S3 and S4 in the supplemental material). The MJO began in November 2015 in a strong phase 3 and transitioned to phase 4 before losing amplitude around 21 November (Fig. S5). It stayed neutral until early December, where the MJO strengthened from a weak phase 4 to a strong phase 4 ten days later. Maintaining a high amplitude, the MJO transitioned through phases 4–8 and reached phase 1 in mid-January 2016. The MJO then weakened slightly before emerging as a midstrength phase 4 event in late January 2016 and moving through phases 5–7.

Of course, since a large fraction of the signal in Fig. 11 seems to come from the ENSO signal, a logical question is why NDJF 2015/16 featured more persistent and intense rainfall in the LPRB than during other major El Niño events (Fig. S4). Previous studies of the SALLJ (e.g., Vera et al. 2006) and the modulation of rainfall in southeastern South America by extratropical transient wave trains during El Niño years emphasize the importance of Pacific–Atlantic interaction for forecasting climate events in this (and other) region(s) (Barreiro 2017).

In particular, a persistent dipolar SST anomaly in the central southern Atlantic Ocean may favor the occurrence of WT 4 by blocking transient extratropical wave activity from the Pacific, facilitating transitions from Chaco jet events (WT 1) to no-Chaco jet events (WT 4) via enhanced low-level wind circulation from southern Brazil toward the Atlantic, and back to northeastern Brazil and the Amazon (see Fig. 12), because of land–sea temperature contrasts. We illustrate a schematic of

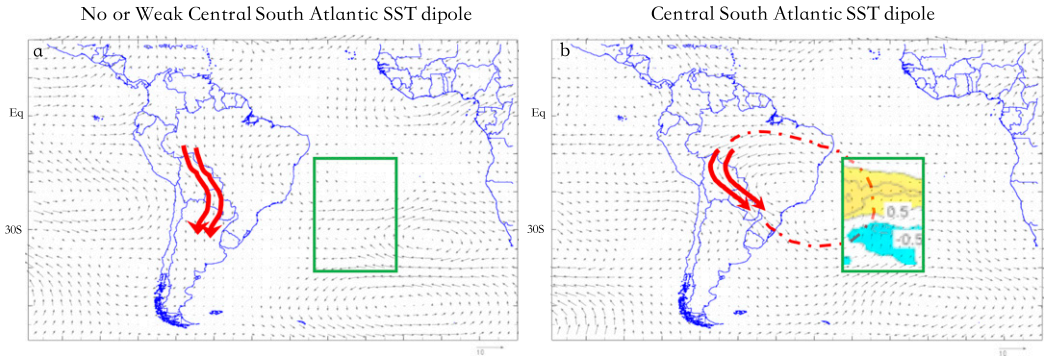

FIG. 12. Schematics of low-level jet events (red arrows) during austral summer and El Niño years. (a) Most jet events are of the Chaco type, particularly when SST anomalies in the central southern Atlantic Ocean (see green box) are weak. (b) When a dipole SST anomaly occurs in the central southern Atlantic with the warmer pole equatorward, the meridional temperature gradient and sea–land temperature contrasts establish an anticyclonic circulation (dot–dashed line) conducive to increased occurrence of no-Chaco jet events. Other SST anomaly configurations tend to be present outside the green box (not shown). Winds (vectors) in (a) and (b) are typical for each case (at 850 hPa; m s^{-1}). Green box shows location of SCAD.

this mechanism in Fig. 12 and note that it is consistent with the mechanism found to produce heavy rainfall in the LPRB (Fig. 4) and with previous studies (e.g., Salio 2002; Liebmann et al. 2004; Vera et al. 2006). We refer to this mechanism as the south central Atlantic dipole (SCAD) and measure it as the mean meridional SST gradient over the box shown in Fig. 12. Examination of the SST anomalies observed during NDJF 2015/16 (Fig. S4) indicates that the mechanism illustrated in Fig. 12 was active, particularly in December 2015 when the most intense rainfall occurred. This suggests that not only did ENSO–MJO conditions favor SALLJ activity, but Atlantic–Pacific interactions specifically favored WT 4 occurrence, helping to explain why the most intense rainfall anomalies occurred specifically in the LPRB.

This Atlantic–Pacific interaction may also help to explain spatial uncertainty in model-based estimates of heavy rainfall in the region. To adequately forecast rainfall in certain parts of southeastern South America during El Niño years, models need to reproduce stationary wave trains originating in the Pacific and the Atlantic and their interactions (Barreiro 2017). Other mechanisms that have been known to modulate rainfall signals in this region include the SACZ (Carvalho et al. 2004; Muñoz et al. 2015, 2016a) and land–biosphere–atmosphere interactions (Grimm et al. 2000, 2007), which also tend to be poorly represented in models (Koster 2004; Green et al. 2017). The stationary wave train interactions, land–atmosphere interactions, and topography may explain why simulating heavy rainfall in this region is so difficult (Figs. 9 and 10). Improving understanding of these phenomena is an important opportunity for S2S prediction and is left for future work.

Finally, it is of interest to consider the link between the observed rainfall events and the observed flooding. Although we motivated this work by describing the impacts of severe flooding in the LPRB, the analysis presented has focused on climate drivers of rainfall. As explained in section 4a, in this region the flat topography (Fig. 1) means that the lower Paraguay River reacts slowly to rainfall (Bravo et al. 2011; Barros et al. 2004), explaining the slow but steady rise in river levels from mid-November 2015 to early January 2016, as shown in Fig. 3. The observed flood peaks during 2015/16 also seem to occur in the context of an active phase of a multidecadal oscillation, possibly associated with low-frequency Pacific activity (Collischonn et al. 2001; Huang et al. 2005). Groundwater dynamics are also important in explaining this behavior (Santos and Lima 2016). Parsing the relative impacts of deforestation and land use changes in the river basin, installation of hydroelectric generation at the Itaipu and Yacyreta Dam sites, river channel modification, antecedent conditions, and climate variability on flood levels will require gathering improved hydrological data and building a comprehensive system model, which is beyond the scope of this paper.

From a policy perspective, reducing flood risk exposure in this region is key to reducing flood losses. Flood events not only in 2015/16 but also in 2014, 2017, and 2018 have caused substantial damage and highlight the need for flood risk management strategies. Doing so will require compiling information on the properties, businesses, and infrastructure that are vulnerable to flooding. This study also suggests that proposed dredging of the upper Paraguay River basin to facilitate navigation could lead to increased summertime streamflow from the upper Paraguay River basin (Pantanal), effectively

coupling the phases of streamflow from the upper and lower Paraguay River basins, which currently have a time delay (Bravo et al. 2011).

7. Summary

In this study we examined the regional climate drivers of the persistent and heavy NDJF 2015/16 rainfall over the lower Paraguay River basin that were associated with severe flood events.

Both enhanced moisture inflow from the low-level jet and convergence associated with baroclinic systems drove the observed heavy rainfall. Repeated SALLJ events, particularly no-Chaco jet events, led to favorable conditions for mesoscale convective activity in this region. Large-scale climate patterns at both seasonal and subseasonal scales favored the synoptic weather patterns observed. Notably, a strong El Niño and an active MJO in phases 4–5 favored SALLJ occurrence. The presence of a dipolar SST anomaly in the central southern Atlantic Ocean also favored the occurrence of no-Chaco jet events.

Numerical forecasts skillfully predicted enhanced risk of heavy rainfall at the seasonal scale, consistent with the observed ENSO signal, but biases in the spatial patterns of forecast rainfall suggest that models imperfectly capture the physical interactions between the Pacific and the Atlantic basins. At subseasonal time scales, uncorrected model forecasts of rainfall had limited skill beyond 15 days, although use of model output statistics—particularly the PCR and CCA methods that correct both spatial patterns and magnitudes—substantially improved forecast skill.

Acknowledgments. The authors thank David Farnham, Upmanu Lall, Laureline Josset, and Andrew Robertson for insightful conversations and guidance. J. D.-G. thanks the NSF GRFP program for support (Grant DGE 16-44869). A. G. M. was supported under award NA14OAR4320106 from the National Oceanic and Atmospheric Administration, U.S. Department of Commerce. The statements, findings, conclusions, and recommendations are those of the authors and do not necessarily reflect the views of the National Oceanic and Atmospheric Administration, or the U.S. Department of Commerce. Streamflow data shown in Fig. 3 were collected by the Paraguayan Navy and National Administration of Navigation and Ports of Paraguay and were processed and distributed by the Paraguayan Directorate of Meteorology and Hydrology (DINAC-DMH). The authors also thank the WWRP/WCRP Subseasonal to Seasonal Prediction Project Database, available via the IRI Data Library mirror at https://iridl.ldeo.columbia.edu/SOURCES/.ECMWF/.S2S/.

REFERENCES

Barnston, A. G., and C. F. Ropelewski, 1992: Prediction of ENSO episodes using canonical correlation analysis. *J. Climate*, **5**, 1316–1345, https://doi.org/10.1175/1520-0442(1992)005<1316:POEEUC>2.0.CO;2.

——, S. Li, S. J. Mason, L. Goddard, D. G. DeWitt, and X. Gong, 2010: Verification of the first 11 years of IRI's seasonal climate forecasts. *J. Appl. Meteor. Climatol.*, **49**, 493–520, https://doi.org/10.1175/2009JAMC2325.1.

——, M. K. Tippett, M. L. L. Heureux, S. Li, and D. G. DeWitt, 2012: Skill of real-time seasonal ENSO model predictions during 2002–11: Is our capability increasing? *Bull. Amer. Meteor. Soc.*, **93**, 631–651, https://doi.org/10.1175/BAMS-D-11-00111.1.

Barreiro, M., 2017: Interannual variability of extratropical transient wave activity and its influence on rainfall over Uruguay. *Int. J. Climatol.*, **37**, 4261–4274, https://doi.org/10.1002/joc.5082.

Barros, V., L. Chamorro, G. Coronel, and J. Baez, 2004: The major discharge events in the Paraguay River: Magnitudes, source regions, and climate forcings. *J. Hydrometeor.*, **5**, 1161–1170, https://doi.org/10.1175/JHM-378.1.

Boers, N., B. Bookhagen, N. Marwan, J. Kurths, and J. Marengo, 2013: Complex networks identify spatial patterns of extreme rainfall events of the South American monsoon system. *Geophys. Res. Lett.*, **40**, 4386–4392, https://doi.org/10.1002/grl.50681.

——, ——, H. M. J. Barbosa, N. Marwan, J. Kurths, and J. A. Marengo, 2014: Prediction of extreme floods in the eastern central Andes based on a complex networks approach. *Nat. Commun.*, **5**, 5199, https://doi.org/10.1038/ncomms6199.

Brakenridge, G., 2016: Global active archive of large flood events. Dartmouth Flood Observatory, https://www.dartmouth.edu/~floods/Archives/index.html.

Bravo, J. M., D. Allasia, A. R. Paz, and W. Collischonn, 2011: Coupled hydrologic-hydraulic modeling of the upper Paraguay River basin. *J. Hydrol. Eng.*, **17**, 635–646, https://doi.org/10.1061/(ASCE)HE.1943-5584.0000494.

British Broadcasting Corporation, 2015: Flooding 'worst in 50 years', as 150,000 flee in Paraguay, Argentina, Brazil and Uruguay. *BBC News*, 27 December, http://www.bbc.com/news/world-latin-america-35184793.

Bröcker, J., and L. A. Smith, 2007: Scoring probabilistic forecasts: The importance of being proper. *Wea. Forecasting*, **22**, 382–388, https://doi.org/10.1175/WAF966.1.

Campetella, C. M., and C. S. Vera, 2002: The influence of the Andes Mountains on the South American low-level flow. *Geophys. Res. Lett.*, **29**, 1826, https://doi.org/10.1029/2002GL015451.

Carbin, G. W., M. K. Tippett, S. P. Lillo, and H. E. Brooks, 2016: Visualizing long-range severe thunderstorm environment guidance from CFSv2. *Bull. Amer. Meteor. Soc.*, **97**, 1021–1031, https://doi.org/10.1175/BAMS-D-14-00136.1.

Carvalho, L. M. V., C. Jones, and B. Liebmann, 2004: The South Atlantic convergence zone: Intensity, form, persistence, and relationships with intraseasonal to interannual activity and extreme rainfall. *J. Climate*, **17**, 88–108, https://doi.org/10.1175/1520-0442(2004)017<0088:TSACZI>2.0.CO;2.

——, A. E. Silva, C. Jones, B. Liebmann, P. L. S. Dias, and H. R. Rocha, 2011a: Moisture transport and intraseasonal variability in the South America monsoon system. *Climate Dyn.*, **36**, 1865–1880, https://doi.org/10.1007/s00382-010-0806-2.

——, C. Jones, A. E. Silva, B. Liebmann, and P. L. Silva Dias, 2011b: The South American Monsoon System and the 1970s climate transition. *Int. J. Climatol.*, **31**, 1248–1256, https://doi.org/10.1002/joc.2147.

Chen, M., W. Shi, P. Xie, V. B. S. Silva, V. E. Kousky, R. Wayne Higgins, and J. E. Janowiak, 2008: Assessing objective techniques for gauge-based analyses of global daily precipitation. *J. Geophys. Res.*, **113**, D04110, https://doi.org/10.1029/2007JD009132.

Collischonn, W., C. E. M. Tucci, and R. T. Clarke, 2001: Further evidence of changes in the hydrological regime of the River Paraguay: Part of a wider phenomenon of climate change? *J. Hydrol.*, **245**, 218–238, https://doi.org/10.1016/S0022-1694(01)00348-1.

Dawson, A., 2016: Windspharm: A high-level library for global wind field computations using spherical harmonics. *J. Open Res. Software*, **4**, e31, http://doi.org/10.5334/jors.129.

Glahn, H. R., and D. A. Lowry, 1972: The use of Model Output Statistics (MOS) in objective weather forecasting. *J. Appl. Meteor. Climatol.*, **11**, 1203–1211, https://doi.org/10.1175/1520-0450(1972)011<1203:TUOMOS>2.0.CO;2.

Goddard, L., W. E. Baethgen, H. Bhojwani, and A. W. Robertson, 2014: The International Research Institute for Climate & Society: Why, what and how. *Earth Perspect.*, **1**, https://doi.org/10.1186/2194-6434-1-10.

Good, I. J., 1952: Rational decisions. *J. Roy. Stat. Soc. London*, **B14**, 107–114, http://www.jstor.org/stable/2984087.

Green, J. K., A. G. Konings, S. H. Alemohammad, J. Berry, D. Entekhabi, J. Kolassa, J.-E. Lee, and P. Gentine, 2017: Regionally strong feedbacks between the atmosphere and terrestrial biosphere. *Nat. Geosci.*, **10**, 410–414, https://doi.org/10.1038/ngeo2957.

Grimm, A. M., 2003: The El Niño impact on the summer monsoon in Brazil: Regional processes versus remote influences. *J. Climate*, **16**, 263–280, https://doi.org/10.1175/1520-0442(2003)016<0263:TENIOT>2.0.CO;2.

——, and R. G. Tedeschi, 2009: ENSO and extreme rainfall events in South America. *J. Climate*, **22**, 1589–1609, https://doi.org/10.1175/2008JCLI2429.1.

——, and M. T. Zilli, 2009: Interannual variability and seasonal evolution of summer monsoon rainfall in South America. *J. Climate*, **22**, 2257–2275, https://doi.org/10.1175/2008JCLI2345.1.

——, V. R. Barros, and M. E. Doyle, 2000: Climate variability in southern South America associated with El Niño and La Niña events. *J. Climate*, **13**, 35–58, https://doi.org/10.1175/1520-0442(2000)013<0035:CVISSA>2.0.CO;2.

——, J. S. Pal, and F. Giorgi, 2007: Connection between spring conditions and peak summer monsoon rainfall in South America: Role of soil moisture, surface temperature, and topography in eastern Brazil. *J. Climate*, **20**, 5929–5945, https://doi.org/10.1175/2007JCLI1684.1.

Hellmuth, M. E., S. J. Mason, C. Vaughan, M. van Aalst, and R. Choularton, 2011: A better climate for disaster risk management. Climate and Society Rep. 3, 118 pp., https://iri.columbia.edu/wp-content/uploads/2013/07/CSP3_Final.pdf.

Herdies, D. L., 2002: Moisture budget of the bimodal pattern of the summer circulation over South America. *J. Geophys. Res.*, **107**, 8075, https://doi.org/10.1029/2001JD000997.

Hoyer, S., and J. Hamman, 2017: Xarray: N-D labeled arrays and datasets in Python. *J. Open Res. Software*, **5**, http://doi.org/10.5334/jors.148.

Huang, H.-P., R. Seager, and Y. Kushnir, 2005: The 1976/77 transition in precipitation over the Americas and the influence of tropical sea surface temperature. *Climate Dyn.*, **24**, 721–740, https://doi.org/10.1007/s00382-005-0015-6.

Hunter, J. D., 2007: Matplotlib: A 2D graphics environment. *Comput. Sci. Eng.*, **9**, 90–95, https://doi.org/10.1109/MCSE.2007.55.

Jolliffe, I. T., and D. B. Stephenson, 2012: *Forecast Verification: A Practitioner's Guide in Atmospheric Science*. 2nd ed., John Wiley & Sons, 292 pp.

Jones, C., and L. M. V. Carvalho, 2002: Active and break phases in the South American monsoon system. *J. Climate*, **15**, 905–914, https://doi.org/10.1175/1520-0442(2002)015<0905:AABPIT>2.0.CO;2.

Kanamitsu, M., W. Ebisuzaki, J. Woollen, S.-K. Yang, J. J. Hnilo, M. Fiorino, and G. L. Potter, 2002: NCEP–DOE AMIP-II reanalysis (R-2). *Bull. Amer. Meteor. Soc.*, **83**, 1631–1643, https://doi.org/10.1175/BAMS-83-11-1631.

Kaplan, A., M. A. Cane, Y. Kushnir, A. C. Clement, M. B. Blumenthal, and B. Rajagopalan, 1998: Analyses of global sea surface temperature 1856–1991. *J. Geophys. Res.*, **103**, 18 567–18 589, https://doi.org/10.1029/97JC01736.

Koster, R. D., 2004: Regions of strong coupling between soil moisture and precipitation. *Science*, **305**, 1138–1140, https://doi.org/10.1126/science.1100217.

Liebmann, B., G. N. Kiladis, C. S. Vera, A. C. Saulo, and L. M. V. Carvalho, 2004: Subseasonal variations of rainfall in South America in the vicinity of the low-level jet east of the Andes and comparison to those in the South Atlantic convergence zone. *J. Climate*, **17**, 3829–3842, https://doi.org/10.1175/1520-0442(2004)017<3829:SVORIS>2.0.CO;2.

Loader, C., 1999: *Local Regression and Likelihood*. Springer, 290 pp.

Marengo, J. A., W. R. Soares, C. Saulo, and M. Nicolini, 2004: Climatology of the low-level jet east of the Andes as derived from the NCEP–NCAR reanalyses: Characteristics and temporal variability. *J. Climate*, **17**, 2261–2280, https://doi.org/10.1175/1520-0442(2004)017<2261:COTLJE>2.0.CO;2.

——, and Coauthors, 2012: Recent developments on the South American monsoon system. *Int. J. Climatol.*, **32**, 1–21, https://doi.org/10.1002/joc.2254.

Marwan, N., and J. Kurths, 2015: Complex network based techniques to identify extreme events and (sudden) transitions in spatio-temporal systems. *Chaos*, **25**, 097609, https://doi.org/10.1063/1.4916924.

Mason, S. J., and O. Baddour, 2008: Statistical modelling. *Seasonal Climate: Forecasting and Managing Risk*, A. Troccoli et al., Eds., Springer, 163–201.

——, and A. P. Weigel, 2009: A generic forecast verification framework for administrative purposes. *Mon. Wea. Rev.*, **137**, 331–349, https://doi.org/10.1175/2008MWR2553.1.

——, and M. K. Tippett, 2017: Climate Predictability Tool version 15.5.10. Columbia University, https://doi.org/10.7916/D8G44WJ6.

McKinney, W., 2010: Data structures for statistical computing in python. *Proc. Ninth Python in Science Conf.*, Austin, TX, SciPy, 51–56, https://conference.scipy.org/proceedings/scipy2010/pdfs/mckinney.pdf.

Messner, J. W., G. J. Mayr, A. Zeileis, and D. S. Wilks, 2014: Heteroscedastic extended logistic regression for postprocessing of ensemble guidance. *Mon. Wea. Rev.*, **142**, 448–456, https://doi.org/10.1175/MWR-D-13-00271.1.

Michelangeli, P.-A., R. Vautard, and B. Legras, 1995: Weather regimes: Recurrence and quasi stationarity. *J. Atmos. Sci.*, **52**, 1237–1256, https://doi.org/10.1175/1520-0469(1995)052<1237:WRRAQS>2.0.CO;2.

Ministerio de Obras Públicas y Comunicación, 2016: Evaluación del impacto de El Niño 2015-2016 en sector transporte y comunicación Paraguay. Tech. Rep., 75 pp.

Moron, V., A. W. Robertson, J.-H. Qian, and M. Ghil, 2015: Weather types across the Maritime Continent: From the diurnal cycle to interannual variations. *Front. Environ. Sci.*, **2**, https://doi.org/10.3389/fenvs.2014.00065.

Muñoz, Á. G., L. Goddard, A. W. Robertson, Y. Kushnir, and W. Baethgen, 2015: Cross–time scale interactions and rainfall extreme events in southeastern South America for the austral summer. Part I: Potential predictors. *J. Climate*, **28**, 7894–7913, https://doi.org/10.1175/JCLI-D-14-00693.1.

——, J. Díaz-Lobatón, X. Chourio, and M. J. Stock, 2016a: Seasonal prediction of lightning activity in north western Venezuela: Large-scale versus local drivers. *Atmos. Res.*, **172–173**, 147–162, https://doi.org/10.1016/j.atmosres.2015.12.018.

——, L. Goddard, S. J. Mason, and A. W. Robertson, 2016b: Cross–time scale interactions and rainfall extreme events in southeastern South America for the austral summer. Part II: Predictive skill. *J. Climate*, **29**, 5915–5934, https://doi.org/10.1175/JCLI-D-15-0699.1.

——, X. Yang, G. A. Vecchi, A. W. Robertson, and W. F. Cooke, 2017: A weather-type-based cross-time-scale diagnostic framework for coupled circulation models. *J. Climate*, **30**, 8951–8972, https://doi.org/10.1175/JCLI-D-17-0115.1.

Nogués-Paegle, J., and K. C. Mo, 1997: Alternating wet and dry conditions over South America during summer. *Mon. Wea. Rev.*, **125**, 279–291, https://doi.org/10.1175/1520-0493(1997)125<0279:AWADCO>2.0.CO;2.

——, L. A. Byerle, and K. C. Mo, 2000: Intraseasonal modulation of South American summer precipitation. *Mon. Wea. Rev.*, **128**, 837–850, https://doi.org/10.1175/1520-0493(2000)128<0837:IMOSAS>2.0.CO;2.

Pedregosa, F., and Coauthors, 2011: Scikit-learn: Machine learning in Python. *J. Mach. Learn. Res.*, **12**, 2825–2830, http://www.jmlr.org/papers/volume12/pedregosa11a/pedregosa11a.pdf.

Reynolds, R. W., N. A. Rayner, T. M. Smith, D. C. Stokes, and W. Wang, 2002: An improved in situ and satellite SST analysis for climate. *J. Climate*, **15**, 1609–1625, https://doi.org/10.1175/1520-0442(2002)015<1609:AIISAS>2.0.CO;2.

Roulston, M. S., and L. A. Smith, 2002: Evaluating probabilistic forecasts using information theory. *Mon. Wea. Rev.*, **130**, 1653–1660, https://doi.org/10.1175/1520-0493(2002)130<1653:EPFUIT>2.0.CO;2.

Salio, P., 2002: Chaco low-level jet events characterization during the austral summer season. *J. Geophys. Res.*, **107**, 4816, https://doi.org/10.1029/2001JD001315.

——, M. Nicolini, and E. J. Zipser, 2007: Mesoscale convective systems over southeastern South America and their relationship with the South American low-level jet. *Mon. Wea. Rev.*, **135**, 1290–1309, https://doi.org/10.1175/MWR3305.1.

Santos, M., and C. Lima, 2016: Identification of structural breaks in hydrological maxima time series in Paraguay River, Pantanal Region, Brazil. *Geophysical Research Abstracts*, Vol. 18, Abstract EGU2016-9467-2, http://meetingorganizer.copernicus.org/EGU2016/EGU2016-9467-2.pdf.

Saulo, C., J. Ruiz, and Y. G. Skabar, 2007: Synergism between the low-level jet and organized convection at its exit region. *Mon. Wea. Rev.*, **135**, 1310–1326, https://doi.org/10.1175/MWR3317.1.

Seluchi, M. E., R. D. Garreaud, F. A. Norte, and A. C. Saulo, 2006: Influence of the subtropical Andes on baroclinic disturbances: A cold front case study. *Mon. Wea. Rev.*, **134**, 3317–3335, https://doi.org/10.1175/MWR3247.1.

van der Walt, S., S. C. Colbert, and G. Varoquaux, 2011: The NumPy array: A structure for efficient numerical computation. *Comput. Sci. Eng.*, **13**, 22–30, https://doi.org/10.1109/MCSE.2011.37.

Velasco, I., and J. M. Fritsch, 1987: Mesoscale convective complexes in the Americas. *J. Geophys. Res.*, **92**, 9591–9613, https://doi.org/10.1029/JD092iD08p09591.

Vera, C., and Coauthors, 2006: The South American Low-Level Jet Experiment. *Bull. Amer. Meteor. Soc.*, **87**, 63–77, https://doi.org/10.1175/BAMS-87-1-63.

Vigaud, N., A. W. Robertson, and M. K. Tippett, 2017: Multimodel ensembling of subseasonal precipitation forecasts over North America. *Mon. Wea. Rev.*, **145**, 3913–3928, https://doi.org/10.1175/MWR-D-17-0092.1.

Vitart, F., and Coauthors, 2017: The Subseasonal to Seasonal Prediction (S2S) Project Database. *Bull. Amer. Meteor. Soc.*, **98**, 163–173, https://doi.org/10.1175/BAMS-D-16-0017.1.

Weijs, S. V., R. van Nooijen, and N. van de Giesen, 2010: Kullback–Leibler divergence as a forecast skill score with classic reliability–resolution–uncertainty decomposition. *Mon. Wea. Rev.*, **138**, 3387–3399, https://doi.org/10.1175/2010MWR3229.1.

Wheeler, M. C., and H. H. Hendon, 2004: An all-season real-time multivariate MJO index: Development of an index for monitoring and prediction. *Mon. Wea. Rev.*, **132**, 1917–1932, https://doi.org/10.1175/1520-0493(2004)132<1917:AARMMI>2.0.CO;2.

Wilks, D. S., 2006: Comparison of ensemble-MOS methods in the Lorenz '96 setting. *Meteor. Appl.*, **13**, 243–256, https://doi.org/10.1017/S1350482706002192.

——, 2009: Extending logistic regression to provide full-probability-distribution MOS forecasts. *Meteor. Appl.*, **16**, 361–368, https://doi.org/10.1002/met.134.